Artificial neural network (ANN) modelling to estimate bubble size from macroscopic image and object features

Luis Vinnett [1], Roberto León [2], Diego Mesa [3]

[1] Department of Chemical and Environmental Engineering, Universidad Técnica Federico Santa María, Valparaíso 2390123, Chile

[2] Department of Computer Science, Universidad Técnica Federico Santa María, Valparaíso 2390123, Chile

[3] Advanced Mineral Processing Research Group, Department of Earth Science and Engineering, Imperial College London, United Kingdom

Corresponding authors: luis.vinnett@usm.cl (L. Vinnett), d.mesa@imperial.ac.uk (D. Mesa)

Abstract: Bubble size measurements in aerated systems such as froth flotation cells are critical for controlling gas dispersion. Commonly, bubbles are measured by obtaining representative photographs, which are then analyzed using segmentation and identification software tools. Recent developments have focused on enhancing these segmentation tools. However, the main challenges around complex bubble cluster segmentation remain unresolved, while the tools to tackle these challenges have become increasingly complex and computationally expensive. In this work, we propose an alternative solution, circumventing the need for image segmentation and bubble identification. An Artificial Neural Network (ANN) was trained to estimate the Sauter mean bubble size (D_{32}) based on macroscopic image features obtained with simple and inexpensive image analysis. The results showed excellent prediction accuracy, with a correlation coefficient, R, over 0.998 in the testing stage, and without bias in its error distribution. This machine learning tool paves the way for robust and fast estimation of bubble size under complex bubble images, without the need of image segmentation.

Keywords: machine learning, artificial neural network, flotation, bubble size, Sauter diameter

1. Introduction

Bubble size is a crucial factor in froth flotation, affecting fundamental phenomena such as bubble-particle interaction (Ahmed & Jameson, 1985; Dai et al., 2000; Tao, 2005; Wang et al., 2016) and froth stability (Calvert & Nezhati, 1987; Cho & Laskowski, 2002; Geldenhuys & McFadzean, 2019; Mesa et al., 2020). These phenomena, in turn, have a substantial impact on flotation kinetics and overall performance. Generally, small bubbles are preferred as they increase the available air-liquid interface, facilitating particle attachment. Bubble size can be controlled in flotation equipment by altering the design of the injector/agitator mechanism (Gorain et al., 1995, 1999; Harris et al., 2005; Kracht et al., 2008; Martín et al., 2008; Mesa & Brito-Parada, 2020; Mesa et al., 2020), and by varying the operating conditions, such frother dosage, air flowrate and impeller speed (Amini et al., 2013; Arancibia-Bravo et al., 2019; Azgomi et al., 2007; Cho & Laskowski, 2002; Grau et al., 2005).

The importance of bubble size distribution in flotation has motivated the development of several measurement methodologies (Couto et al., 2009; Junker, 2006; Kracht & Moraga, 2016; Lichti & Bart, 2018; Prasser et al., 2001), among which the most widely used corresponds to the utilization of bubble viewer apparatuses (Chen et al., 2001; Grau & Heiskanen, 2002; Hernandez-Aguilar et al., 2002; Vazquez et al., 2005). This methodology entails the sampling of bubbles from the pulp using a sampling tube into a viewing chamber, where bubbles are photographed. The images are analyzed using image analysis tools to identify, segment and measure each individual bubble (Bailey et al., 2005; Kracht et al., 2013; Mesa et al., 2022; Vinnett et al., 2018; Vinnett et al., 2020). Although the strategy of bubble segmentation and identification has been successful, there persist challenges associated with: (i) the computational cost of complex segmentation algorithms; (ii) the correct and unbiased segmentation of complex bubble

clusters (Karn et al., 2015; Kracht et al., 2013; Ma et al., 2014; Vinnett, 2023); and (iii) the identification of large non-convex bubbles, in the absence of stereological information. Bubble identification from automated image analysis has proven to be erratic for industrial conditions (Vinnett, 2023), especially under the presence of large and small bubbles in the same population.

In addition to conventional techniques such as Watershed and Hough transforms, machine learning has emerged as a valuable tool for enhanced bubble segmentation and identification. Among the different machine-learning techniques used for image-analysis problems in mineral processing, Convolutional Neural Networks (CNN) have been extensively studied. CNNs have proven to be superior to traditional computer vision methods for image segmentation, achieving high resolution (He et al., 2020; Hessenkemper et al., 2022). Various CNN approaches have been explored for bubble segmentation, such as the use of region-based CNNs like Faster-RCNN (Haas et al., 2020), sliding window-based CNN (Poletaev et al., 2020), and the implementation of segmentation masks through Mask RCNN, which not only classifies but also assigns each pixel to individual bubble objects (Cui et al., 2021; Hessenkemper et al., 2022; Kim & Park, 2021; Wang et al., 2023). Although significant progress made with CNN-based techniques has been made in recent years, challenges persist in segmenting very complex images, such as those obtained in industrial settings, which are typically subject to wide bubble-size distributions, high gas content, cloudiness due to the presence of solid particles, and lighting issues.

In many mineral processing applications, precise segmentation for the identification of each individual bubble may not be necessary. Instead, froth flotation models often use average metrics such as the Sauter mean diameter ($D_{32} = \Sigma d_{b,i}^3 / \Sigma d_{b,i}^2$) to correlate gas dispersion with metallurgical performance. Therefore, alternative approaches to directly estimate D_{32} can suffice for practical purposes. Innovative alternative strategies have been proposed, using algorithms that do not focus on segmenting and identifying individual bubbles, but instead strive to estimate the bubble size distribution or its Sauter mean for the entire image. For instance, Kracht et al. (2013) proposed a stochastic method using image background covariance for bubble size distribution (BSD) determination, which was validated in laboratory tests and simulations. Similarly, Vinnett and Alvarez-Silva (2015) established a linear model connecting shadow percentage in binary bubble images to D_{32}, using varying gas rates. The latter was refined by Vinnett, Cornejo, et al. (2022), where a linear model was determined between D_{32} and over 12 image properties obtained automatically, without bubble segmentation, resulting in a fast and accurate estimation of the Sauter diameters in the range of 1.3–6.7 mm.

This work seeks to establish a connection between traditional and modern approaches to estimating bubble size, employing an Artificial Neural Network (ANN) to autonomously determine relationships between image properties and the Sauter mean diameter of bubble populations. Although several image analysis applications based on CNNs have proven to outperform ANNs (Bu et al., 2022), ANNs are still powerful tools in parameter-based modelling when there exist strong levels of association between input and output variables (Bishop, 2006). ANNs are well-suited for processing structured information, such as tabular data, with fully connected layers, offering versatility across various data types. Artificial neural networks have been extensively used in mineral processing research. However, the application of ANN to assess gas dispersion in flotation has been rather scarce, and mainly employed in the development of soft sensors from operating conditions, rather than from image properties. For instance, Massinaei and Doostmohammadi (2010) applied an ANN to predict the bubble surface area flux (S_B), using the superficial gas velocity (J_G), frother dosage, and solid content as predictors. Similarly, Bhunia et al. (2015) used an ANN to estimate the gas holdup in a flotation tank based on the J_G, solid content, frother type and slurry feed rate.

In this work, however, the ANN was not directly used as a soft sensor, but as a tool to streamline the analysis of bubble images. To the authors' knowledge, this is the first ANN to characterize bubble size from macroscopic images and object features for practitioners who use bubble viewers along with image analysis to characterize gas dispersion. By avoiding the challenges of complex segmentation algorithms, we aim to offer a practical solution for quickly and accurately estimating D_{32} from bubble images using machine learning, given an adequate training database.

2. Materials and Methods

The experimental setup and methods associated with the bubble acquisition using a McGill bubble size analyser, as well as their initial analysis using a semi-automated tool, are well described by Vinnett, Cornejo, et al. (2022). A summary is provided here for completeness.

The D_{32} values obtained with the semi-automated tool was used as ground truth. The image descriptors obtained in a fully automated image analysis step were randomly divided into training and testing datasets for building and training an Artificial Neural Network capable of estimating D_{32}. Fig. 1 graphically describes the methodology used in this work.
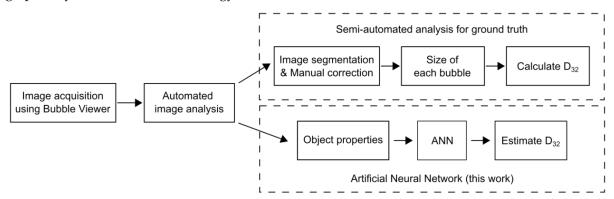

Fig. 1. Diagram of the data flow and estimation methodology used in this work. The semi-automated system was used to obtain the ground truth for D_{32}. An artificial neural network was trained to estimate the D_{32} based on the object properties obtained from an automated image analysis without segmentation.

2.1. Experimental setup

Bubble size measurements were conducted in a laboratory-scale flotation cell that replicates a cross-section of an industrial machine, as described in Vinnett et al. (2022) (see Fig. 2). Bubble sampling was performed using a McGill bubble size analyser (MBSA) (Hernandez-Aguilar et al., 2002). The rising bubbles were photographed at a rate of one frame per second. All measurements were taken over 3 minutes at a resolution of 0.056 mm/pixel.

Four types of frothers were examined: methyl isobutyl carbinol (MIBC, purity ≥ 98.5% by weight), AeroFroth® 70 (Cytec, Woodland Park, NJ, USA), OrePrep® F-507 (Cytec, Wood-land Park, NJ, USA), and Flotanol® 9946 (Clariant Mining Solutions, Louis-ville, KY, USA). AeroFroth® 70 contains MIBC (≥ 98% by weight) and diisobutyl ketone (≤ 2% by weight) (Solvay, 2018), OrePrep® F-507 contains glycol and other non-hazardous components (Saavedra Moreno et al., 2022), and Flotanol® 9946 corresponds to a 2-ethyl hexanol distillation bottom (Arends, 2019). Table 1 details the experimental conditions, including frother concentrations and superficial gas rates. The MIBC experiments were conducted at two locations. At J_G = 2.5 cm/s, some churn-turbulent conditions were detected and removed from the analysis based on the methodology reported by Vinnett, Yianatos, et al. (2022). For AeroFroth® 70, OrePrep® F-507, and Flotanol® 9946, 5 repetitions were conducted at J_G = 0.4 cm/s, and 3 at J_G = 1.2 cm/s and 2.0 cm/s. No repetitions were conducted at J_G = 0.8 cm/s and 1.6 cm/s. In all measurements, the MBSA was filled with conditioned water at the same frother concentration as the flotation cell to prevent bubble coalescence. Two hundred and seventy-nine experimental conditions were run and analyzed.

2.2. Semi-automated image processing

To obtain the ground truth for the Sauter mean bubble size, the images were analysed using a traditional identification and segmentation method, along with a manual correction step. To this end, the bubble size analysis was performed using the semi-automated tool introduced by Vinnett et al. (2009) and updated by Vinnett (2023), based on the Image Processing Toolbox of MATLAB (11.4, The MathWorks Inc., Natick, MA, USA). A field of view measuring 45 × 35 mm was selected for image analysis.
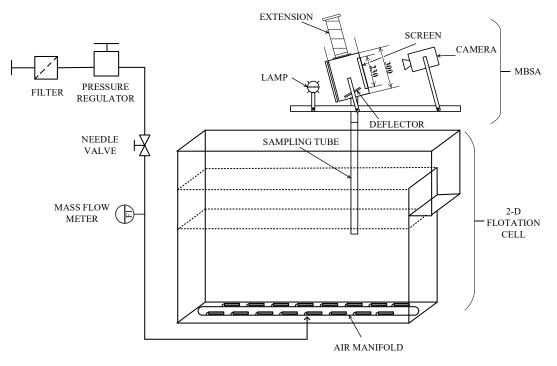
Fig. 2. Two-dimensional flotation cell and installation of the McGill bubble size analyser
(Vinnett, Cornejo, et al., 2022)

Table 1. Experimental conditions

Type of Frother	Frother Concentrations, ppm	Superficial Gas Rates, cm/s
MIBC	0, 2, 4, 8, 16	0.5, 1.0, 1.5, 2.0, 2.5
AeroFroth® 70	0, 2, 4, 8, 16, 32	0.4, 0.8, 1.2, 1.6, 2.0
OrePrep® F-507	0, 2, 4, 8, 16, 32	0.4, 0.8, 1.2, 1.6, 2.0
Flotanol® 9946	0, 2, 4, 8, 16, 32	0.4, 0.8, 1.2, 1.6, 2.0

In this semi-automated tool, the images are initially converted into binary representations, where isolated spheres and ellipsoids are automatically identified based on solidity. Objects with low solidity are then automatically segmented/identified using Watershed and Hough transforms. Individual bubble sizes can be estimated as equivalent ellipsoid diameters from the object axes.

Manual processing corrected false positives in the fully automated image analysis and allowed for the characterization of non-identified bubbles. This procedure prevented biases caused by removing bubbles from the analysis. Manual and automated segmentation assumed that the observed clusters in the region of interest are mostly justified by collisions in the MBSA chamber, rather than bubble coalescence. These collisions are intensified by the deflector glass of the MBSA, which aids the bubbles to be photographed in a 2D plane (Vinnett, Urriola, et al., 2022). It should be noted that other approaches may have been used to define the ground truth (*e.g.*, synthetic bubbles). However, the semi-automated approach presented here has proven to be robust in the bubble size characterization at both laboratory and industrial scales (Vinnett, 2023). The latter being more challenging due to the higher probability of photographing cap-shaped bubbles at higher superficial gas rates.

The D_{32} values obtained from this semi-automated method were used as the ground truth to evaluate the predictive ability of the ANN to estimate bubble size. A subset of 180 images per experimental condition was randomly chosen, processing a minimum of 1500 bubbles per test. However, at least 10 images were processed in all cases. This limitation for the number of processed images was especially defined for conditions with high gas hold-up.

All images were analysed when operating the cell without frother. For detailed information on the semi-automated procedure, please refer to Vinnett (2023). Fig. 3 illustrates an image processed by the semi-automated approach, in which bubbles highlighted by their border (or best ellipse) were automatically detected. Bubbles highlighted by crosses were manually identified.
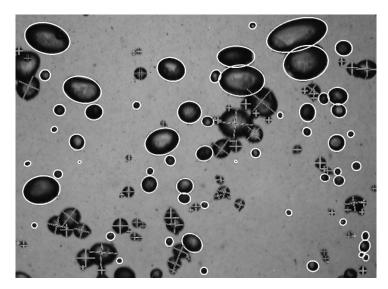
Fig. 3. Example of an image processed by the semi-automated procedure

2.3. Region properties and their association with bubble size

The region properties of the binary images analysed by the fully automated method were obtained. These properties were used as inputs in the ANN modelling to predict the Sauter diameter. An example of an analysed image is shown in Fig. 4(a), from which the object and region properties summarized in Table 2 were calculated.

For all processed images, the median and different indicators of variability were estimated for the evaluated properties (e.g., circularity, solidity, aspect ratio, perimeter). Most of the object features were obtained from the Image Processing Toolbox of MATLAB (11.4, The MathWorks Inc., Natick, MA, USA), using the regionprops function. Circularities, aspect ratios, eccentricities, perimeters, solidities, equivalent diameters, and the number of objects per mm² were obtained from this tool.

The spatial bandwidths and the shadow fractions were also calculated for each processed image. The spatial bandwidth indirectly indicates the average pulse width generated by the black pixels. In the example of Fig. 4(a), the pulses are related to the disturbances of bubbles over the grey line. For the signals associated with these trains of pulses, the bandwidth was obtained at −20 dB with respect to the peak in the power spectral density, as illustrated in Fig. 4(b) (Vinnett et al., 2018). The shadow fraction corresponds to the ratio between the overall area of the black regions with respect to the area of the entire region of interest.

Table 3 indicates the nomenclature for each studied feature. The median along with one variability index per object or region property were used as descriptors to estimate D_{32}. The variability index per feature was chosen from the relative standard deviation (subscript RSD), relative interdecile range (subscript RIDR), relative interquintile range (subscript RIQQR), and relative interquartile range (subscript RIQR), based on the highest level of association with the D_{32} values (Vinnett, Cornejo, et al., 2022).

Table 2. List of studied region and object properties.

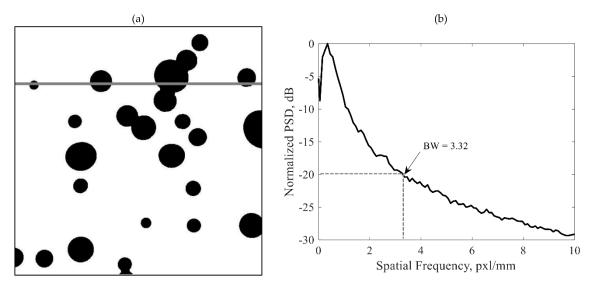| Property	Variable Symbol	Statistical Index
Shadow Fraction	SF	
Circularity, $4\pi\ \mathbf{area}/P^2$	C	
Aspect Ratio, *major axis length/minor axis length*	AR	Median
Eccentricity	E	Relative Standard Deviation
Perimeter, mm	P	Relative Interdecile Range
Solidity	S	Relative Interquintile Range
Equivalent Diameter, $\sqrt{4\ \mathbf{area}/\pi}$, mm	ED	Relative Interquartile Range
Number of Objects per mm², 1/mm²	N	
Spatial Bandwidth, pxl/mm	BW	

Fig. 4. (a) Example of binary image, and (b) normalized power spectral density and bandwidth estimation (Vinnett et al., 2018)

2.3. Artificial neural network

An Artificial Neural Network was employed to establish relationships between image properties of Table 2 and the Sauter mean diameter of the bubble populations. The values for the D_{32} ground-truth corresponded to those obtained from the semi-automated procedure. The network architecture comprised a single hidden layer housing 8 neurons. The input layer incorporated 18 image and object descriptors: the median and a measure of dispersion for the 9 properties listed in Table 2. The architecture of the ANN is conceptualised in Fig. 5.

The activation function Rectified Linear Unit (ReLu) (Schmidhuber, 2015) was applied between the input and the hidden layer, fostering non-linearity for modelling purposes. A Linear activation function was utilized for the output layer to obtain the D_{32} values. Prior to training, all descriptors underwent standardization. The network weights were initialized using the *He uniform* method (He et al., 2015). The Adam optimizer (Kingma & Ba, 2014), with a learning rate of 0.001, was employed to minimize the mean squared error in the training stage. The network and learning settings were defined in a previous grid search stage.

For training and evaluation, the dataset was randomly split, with 70% of the data (195 descriptors-D_{32} datasets) being used for training the ANN and the remaining 30% (84 descriptors-D_{32} datasets) reserved for testing its predictive capacity. The ANN underwent training for 300 epochs with a batch size of 10. The training and testing procedures were repeated 1000 times, randomly selecting the 70/30 training-testing subsets each time, to evaluate the robustness of the ANN. Thus, the sensitivity of the ANN results to influential observations in the training process was assessed. All ANN algorithms were implemented in Python 3 (Van Rossum, G., & Drake, F. L., Scotts Valley, CA, USA).

2.5. Blind tests

Blind tests were performed, assessing the response of the ANN to new data with considerably different conditions or settings to the training datasets. The objective of this analysis was the evaluation of the ANN model's robustness for extending its application in different conditions.

Two "external" datasets were evaluated. The first one corresponds to 9 experimental sets obtained in a 85.5 cm × 9.8 cm (L × D) cylindrical column operated with one porous sparger. Moreover, these experiments were performed using an alternative frother to those described in Table 1, namely Flottec F120-20, with a purity of 99.5% by weight (Flottec, 2015). The bubbles were generated at J_G of 0.4, 1.2 and 2.0 cm/s, and with frother concentrations of 0, 4 and 32 ppm. Bubble images were obtained using the same methodology as that described in Section 2.1.

The second dataset corresponds to industrial data from 15 mechanical cells corresponding to rougher (42.5 m³ and 127 m³), first cleaner (28. 3 m³ and 42.5 m³) and scavenger (14.2 m³ and 28. 3 m³) stages,

and 4 industrial columns (a second cleaner stage, 2 m × 8 m × 10 m), corresponding to 19 different operating conditions. All industrial data were obtained in a Cu/Mo Chilean concentrator.

These datasets were analysed with the automatic tool to obtain the object properties (e.g., Fig. 4) required to predict the D_{32} values from the ANN model. These datasets were not included in the ANN training process. The semi-automated tool (Section 2.2) was also used to determine the ability of the automated ANN to estimate D_{32} values comparable to those obtained from a tool that did not remove irregular bubbles nor bubbles in clusters.
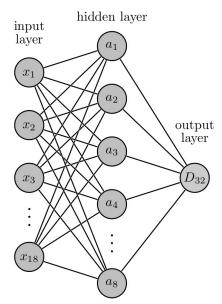

Fig. 5. ANN architecture: an input layer with 18 neurons, a hidden layer with 8 neurons, and an output layer with the D_{32} estimation

3.   Results and discussion

3.1.   ANN training, validation, and comparison with a linear model

The ANN was trained and tested, using 70% of the data for the former and 30% for the latter. The semi-automated D_{32} results were used as a reference (ground truth) for comparison purposes. To evaluate the robustness of the network, 1000 training-testing subsets were randomly chosen and assessed. From these 1000 results, the network ability to estimate D_{32} was evaluated, using the correlation coefficient, *R*, as an indicator. Fig. 6 shows the cumulative distribution function of the *R* values obtained from the testing subsets, compared to those obtained from the linear model proposed by Vinnett, Cornejo, et al. (2022). Although both models have an excellent response, the ANN consistently outperforms the linear model, exhibiting *R* values mostly greater than 0.995, which indicates a suitable generalization of the D_{32} estimations. Only 3% of the testing subsets presented an *R*-value lower than 0.993 with the ANN modelling, indicating the potential of this tool to characterize D_{32}.

Fig. 7 illustrates the modelling performance for the training and testing subsets, considering the percentiles 2.5 [Fig. 7(a)], 50 [Fig. 7(b)] and 97.5 [Fig. 7(c)] for the coefficient of correlation obtained from the latter subset. The ANN allowed for an adequate description of the training and testing subsets. Even at low percentiles for the R value in the testing procedure [Fig. 7(a)], the network was able to represent the D_{32} variability for datasets not involved in the training stage.

Results from Fig. 7 proved the low sensitivity of the ANN model to different training-testing subsets, which again highlights the robustness of the model structure of Fig. 5. For the three testing conditions depicted in Fig. 7, the D_{32} errors with respect to the semi-automated D_{32} estimations were analysed for the automated image processing and the ANN modelling. These D_{32} errors were calculated by subtracting the semi-automated D_{32} values from the automated image analysis and ANN D_{32} estimates.

Fig. 8 presents the cumulative distribution functions of the D_{32} errors, showing the results associated with the percentiles 2.5 [Fig. 8(a)], 50 [Fig. 8(b)] and 97.5 [Fig. 8(c)] of the R values obtained when testing the network. The variability of the D_{32} errors obtained from the automated and ANN approaches were
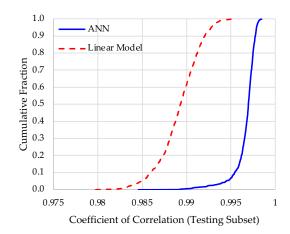
Fig. 6. Comparison of the cumulative distribution functions of the coefficient of correlation from the testing subsets: the ANN model versus the linear model proposed by Vinnett, Cornejo, et al. (2022)
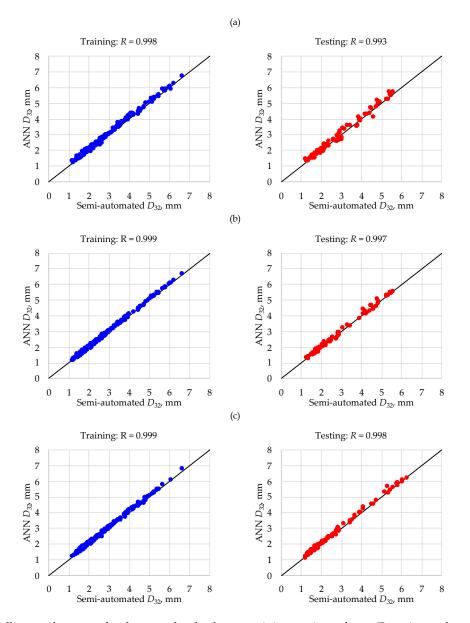

Fig. 7. Modelling performance for three randomly chosen training-testing subsets. Experimental conditions that led to the (a) 2.5, (b) 50, and (c) 97.5 percentiles for correlation coefficient in the testing subsets. The datapoints represent the experimental data, whereas the continuous line corresponds to the ideal trend $y = x$
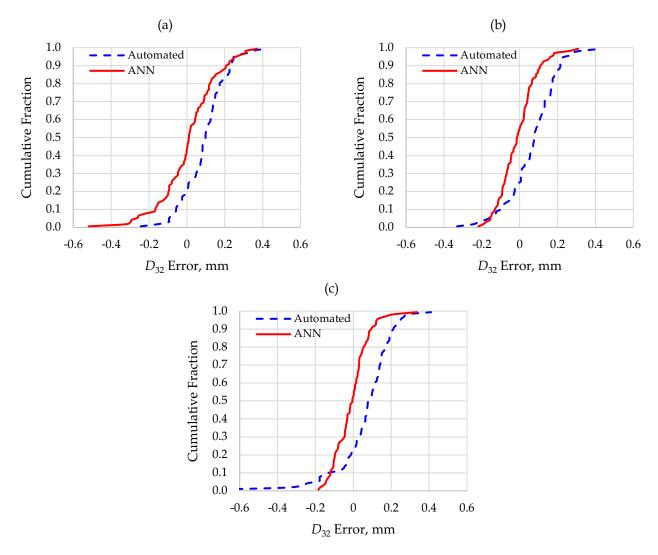
Fig. 8. Cumulative distribution functions of the D_{32} errors from the automated image processing and the ANN estimations. Experimental conditions that led to the (a) 2.5, (b) 50, and (c) 97.5 percentiles for correlation coefficient in the testing subsets

comparable in magnitude. However, biased results were obtained from the automated image analysis, with error distributions shifted towards positive values in all cases. Thus, the automated image processing overestimated the D_{32} values despite the high coefficient of correlation with respect to the semi-automated estimations (R = 0.993) (Vinnett, 2023). Conversely, non-biased results were obtained from the ANN for the testing subsets.

Table 3 presents the 95% confidence intervals of the mean of the D_{32} errors from the automated image processing and ANN estimations, for the three conditions shown in Fig. 8. A consistent positive bias was obtained from the automated image analysis. This bias was mainly justified by the presence of false-positives at D_{32} values lower than 3.0 mm, which were attributed to misidentified clusters as single bubbles. As the 95% confidence intervals of the mean for the D_{32} errors crossed zero in all cases, non-significant bias was observed with the ANN modelling. This result implied that the model structure of Fig. 5 allowed for better results than those obtained from automated image analysis, given a representative D_{32} database and an adequate set of descriptors to train the network.

3.2. Blind test with laboratory- and industrial-scale data

Two blind tests were performed, in which the previously trained ANN was tested with lab-scale and industrial-scale datasets with conditions that considerably differed from the training stage (see Section
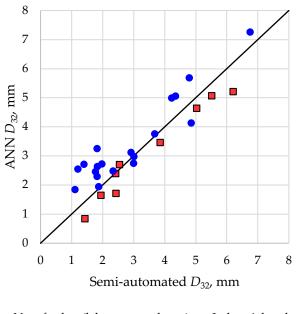
2.5). Fig. 9 presents the D_{32} estimations, showing that the ANN was able to detect the bubble size variability for datasets beyond those employed for training.

For the lab-scale flotation column operated with the F120-20 frother, the coefficient of correlation between the measured and predicted D_{32} values resulted $R = 0.981$, whereas an R value of 0.93 was obtained from industrial data including mechanical cells and flotation columns. Higher uncertainties are observed due to the difference in the object features measured in the different flotation systems. In addition, some bias was obtained, with the ANN overestimating the Sauter diameter for the industrial data and underestimating the D_{32} values for the lab-scale flotation column. The presence of solids in the industrial images may also have affected the accuracy and precision of the D_{32} predictions.

It should be noted that automated image analysis from conventional tools has led to erratic responses for industrial datasets as reported in (Vinnett, 2023). To the authors' knowledge, no automated image analysis tools have proven to be robust in the analysis of non-ideal bubble images, and further developments must be made on this subject.

Table 3. Confidence intervals of the mean of the D_{32} errors at 95% level obtained from the automated and ANN estimations. Experimental conditions that led to the 2.5, 50 and 97.5 percentiles for correlation coefficient in the testing subsets

D_{32} Errors	Percentiles for the Correlation Coefficient in the Testing Datasets, ANN		
	2.5	50	97.5
Automated D_{32} Estimation	0.068 – 0.118	0.040 – 0.096	0.030 – 0.098
ANN D_{32} Estimation	−0.023 – 0.044	−0.031 – 0.012	−0.029 – 0.010

Fig. 9. Blind test: modelling performance using datasets with different characteristics to the training datasets. The red squares represent the results obtained using laboratory-scale data in a flotation column operated with a different frother (Flottec F120-20). The blue circles represent the results obtained from industrial-scale data. The continuous line corresponds to the ideal trend y = x

The results obtained in this study established the efficacy of our ANN model in achieving accurate and unbiased estimations of bubble size for a specific flotation system, relying solely on macroscopic image and object features. This model circumvents the need for algorithms for complex cluster segmentation, streamlining the Sauter mean estimation process. Moreover, results from Fig. 9 show the potential for using this ANN approach to estimate D_{32} in cases outside the training data, including the

analysis of complex industrial cases. The strong level of association between D_{32} and the macroscopic image and object properties reported by Vinnett, Cornejo, et al. (2022) made the proposed ANN suitable to estimate bubble size in the studied flotation systems.

Future work should focus on expanding the training database, incorporating images as ground truth from diverse laboratory, pilot, and industrial scenarios at different operating conditions. It is expected that a synergy between machine learning approaches can be leveraged, utilising the training masks generated by segmentation algorithms such as Mask R-CNN as ground truths. This database holds the promise of expediting the accurate estimation of bubble size by simply extracting macroscopic image features, in which bubble identification and object segmentation will only be required in the training stages.

4. Conclusions

This study introduced an Artificial Neural Network (ANN) model for the efficient and reliable estimation of the Sauter mean diameter (D_{32}) in flotation. In contrast to conventional methodologies, this approach uses basic image analysis to obtain macroscopic image and object properties, without the need of complex algorithms for image segmentation. Two hundred and seventy-nine experimental conditions were used to train and test the ANN, relating different image properties with the expected D_{32} values. The latter were obtained from a semi-automated procedure to avoid biases caused by misidentified bubbles. From the D_{32} estimations and comparisons, the following conclusions were obtained:

- The ANN was remarkably robust, with high correlation coefficients in the testing stage ($R > 0.998$) across diverse training-testing subsets. Its low sensitivity to variations in the training-testing selections highlights its efficacy in capturing D_{32} variability, even for non-observed datasets during training.
- Compared to automated image processing, the ANN showed superior performance, providing non-biased and more accurate D_{32} estimates from the testing subsets.
- The positive bias observed with the automated approach was attributed to misidentified clusters, emphasizing the ANN potential for overcoming challenges associated with segmentation algorithms.
- The predictive capacity of the ANN was evaluated, estimating D_{32} values for laboratory and industrial conditions that were not used in the training-testing stages. Although some bias was observed, the results proved the potential of the proposed approach to estimate D_{32} at different scales. The need for more diverse training databases was highlighted from this analysis.

These findings offered a practical and swift solution for D_{32} estimation, addressing critical issues in bubble size characterization. Further exploration of ANN applications is encouraged, emphasizing the need for extensive training databases under diverse operational conditions and experimental settings.

Acknowledgments

References

AHMED, N., JAMESON, G. J., 1985. *The effect of bubble size on the rate of flotation of fine particles*. Int. J. Miner. Process. 14(3), 195-215.

AMINI, E., BRADSHAW, D. J., FINCH, J A., BRENNAN, M., 2013. *Influence of turbulence kinetic energy on the bubble size in different scale flotation cells*. Miner. Eng. 45, 146-150.

ARANCIBIA-BRAVO, M. P., LUCAY, F. A., LÓPEZ, J., CISTERNAS, L. A., 2019. *Modeling the effect of air Flow, impeller speed, frother dosages, and salt concentrations on the bubbles size using response surface methodology*. Miner. Eng. 132, 142-148.

ARENDS, M. A., 2019. *Reactivos de flotación: Evaluación de colectores y espumantes*. Clariant: Muttenz, Switzerland.

AZGOMI, F., GOMEZ, C. O., FINCH, J. A., 2007. *Correspondence of gas holdup and bubble size in presence of different frothers*. Int. J. Miner. Process. 83(1), 1-11.

BAILEY, M., GOMEZ, C. O., FINCH, J. A., 2005. *Development and application of an image analysis method for wide bubble size distributions*. Miner. Eng. 18(12), 1214-1221.

BHUNIA, K., KUNDU, G., MUKHERIEE, D., 2015. *Prediction of Gas Holdup in a Flotation Column by Artificial Neural Network*. Int. J. Coal Prep. Util. 35(4), 165-175.

BISHOP, C. M., 2006. *Pattern Recognition and Machine Learning* (*Information Science and Statistics*). Springer-Verlag, Berlin, Heidelberg.

BU, X., ZHOU, S., DANSTAN, J. K., BILAL, M., UL HASSAN, F., & CHAO, N., 2022. *Prediction of coal flotation performance using a modified deep neural network model including three input parameters from feed*. Energy Sources A: Recovery Util. Environ. Eff. 1-13.

CALVERT, J. R., NEZHATI, K., 1987. *Bubble size effects in foams*. Int. J. Heat Fluid Flow 8(2), 102-106.

CHEN, F., GOMEZ, C. O., FINCH, J. A., 2001. *Technical note bubble size measurement in flotation machines*. Miner. Eng. 14(4), 427-432.

CHO, Y. S., LASKOWSKI, J. S., 2002. *Effect of flotation frothers on bubble size and foam stability*. Int. J. Miner. Process. 64(2), 69-80.

COUTO, H. J. B., NUNES, D. G., NEUMANN, R., FRANÇA, S. C. A., 2009. *Micro-bubble size distribution measurements by laser diffraction technique*. Miner. Eng. 22(4), 330-335.

CUI, Y., LI, C., ZHANG, W., NING, X., SHI, X., GAO, J., LAN, X., 2022. *A deep learning-based image processing method for bubble detection, segmentation, and shape reconstruction in high gas holdup sub-millimeter bubbly flows*, Chem. Eng. J. 449, 137859.

DAI, Z., FORNASIERO, D., RALSTON, J., 2000. *Particle-bubble collision models – a review*. Adv. Colloid Interface Sci. 85(2), 231-256.

FLOTTEC, 2015. *Flottec F120-20 Frother*, Safety Datasheet.

GELDENHUYS, S., MCFADZEAN, B., 2019. *The effect of pulp bubble size on the dynamic froth stability measurement*. Miner. Eng. 131, 164-169.

GORAIN, B. K., FRANZIDIS, J. P., MANLAPIG, E. V., 1995. *Studies on impeller type, impeller speed and air flow rate in an industrial scale flotation cell – Part 1: Effect on bubble size distribution*. Miner. Eng. 8(6), 615-635.

GORAIN, B. K., FRANZIDIS, J. P., MANLAPIG, E. V., 1999. *The empirical prediction of bubble surface area flux in mechanical flotation cells from cell design and operating data*. Miner. Eng. 12(3), 309-322.

GRAU, R. A., HEISKANEN, K., 2002. *Visual technique for measuring bubble size in flotation machines*. Miner. Eng. 15(7), 507-513.

GRAU, R. A., LASKOWSKI, J. S., HEISKANEN, K., 2005. *Effect of frothers on bubble size*. Int. J. Miner. Process. 76(4), 225-233.

HAAS, T., SCHUBERT, C., EICKHOFF, M., PFEIFER, H., 2020. *BubCNN: Bubble detection using Faster RCNN and shape regression network*. Chem. Eng. Sci. 216, 115467.

HARRIS, R., NG, K. W., WRAITH, A. E., 2005. *Spargers for controlled bubble size by means of the multiple slot disperser (MSD)*. Chem. Eng. Sci. 60(11), 3111-3115.

HE, K., GKIOXARI, G., DOLLÁR, P., GIRSHICK, R., 2020. *Mask R-CNN*. PAMI 42(2), 386-397.

HE, K., ZHANG, X., REN, S., SUN, J., 2015. *Delving Deep into Rectifiers: Surpassing Human-Level Performance on ImageNet Classification*. IEEE International Conference on Computer Vision.

HERNANDEZ-AGUILAR, J., GOMEZ, C., FINCH, J., 2002. *A technique for direct measurement of bubble size distributions in industrial flotation cells*. 34th Annual Meeting of the Canadian Mineral Processors.

HESSENKEMPER, H., STARKE, S., ATASSI, Y., ZIEGENHEIN, T., LUCAS, D., 2022. *Bubble identification from images with machine learning methods*. Int. J. Multiph. Flow, 155, 104169.

JUNKER, B., 2006. *Measurement of bubble and pellet size distributions: past and current image analysis technology*. Bioproc. Biosyst. Eng. 29(3), 185-206.

KAM, A., ELLIS, C., ARNDT, R., HONG, J., 2015. *An integrative image measurement technique for dense bubbly flows with a wide size distribution*. Chem. Eng. Sci. 122, 240-249.

KIM, Y., PARK, H., 2021. *Deep learning-based automated and universal bubble detection and mask extraction in complex two-phase flows*. Sci. Rep. 11(1), 8940.

KINGMA, D. P., BA, J., 2014. *Adam: A Method for Stochastic Optimization*. arXiv, arXiv:1412.6980.

KRACHT, W., EMERY, X., PAREDES, C., 2013. *A stochastic approach for measuring bubble size distribution via image analysis*. Int. J. Miner. Process. 121, 6-11.

KRACHT, W., GOMEZ, C. O., FINCH, J. A., 2008. *Controlling bubble size using a frit and sleeve sparger*. Miner. Eng. 21(9), 660-663.

KRACHT, W., MORAGA, C., 2016. *Acoustic measurement of the bubble Sauter mean diameter d_{32}*. Miner. Eng. 98, 122-126.

LICHTI, M., BART, H.-J., 2018. *Bubble size distributions with a shadowgraphic optical probe*. Flow Meas. Instrum. 60, 164-170.

MA, Y., YAN, G., SCHEUERMANN, A., BRINGEMEIER, D., KONG, X.-Z., LI, L., 2014. *Size distribution measurement for densely binding bubbles via image analysis*. Exp. Fluids 55(12), 1860.

MARTÍN, M., MONTES, F. J., GALÁN, M. A., 2008. *Bubbling process in stirred tank reactors I: Agitator effect on bubble size, formation and rising*. Chem. Eng. Sci. 63(12), 3212-3222.

MASSINAEI, M., DOOSTMOHAMMADI, R., 2010. *Modeling of bubble surface area flux in an industrial rougher column using artificial neural network and statistical techniques*. Miner. Eng. 23(2), 83-90.

MESA, D., BRITO-PARADA, P. R., 2020. *Bubble size distribution in aerated stirred tanks: Quantifying the effect of impeller-stator design*. Chem. Eng. Res. Des. 160, 356-369.

MESA, D., MORRISON, A. J., BRITO-PARADA, P. R., 2020. *The effect of impeller-stator design on bubble size: Implications for froth stability and flotation performance*. Miner. Eng. 157, 106533.

MESA, D., QUINTANILLA, P., REYES, F., 2022. *Bubble Analyser − An open-source software for bubble size measurement using image analysis*. Miner. Eng. 180, 107497.

POLETAEV, I., TOKAREV, M. P., PERVUNIN, K. S., 2020. *Bubble patterns recognition using neural networks: Application to the analysis of a two-phase bubbly jet*, Int. J. Multiph. Flow 126, 103194.

PRASSER, H. M., SCHOLZ, D., ZIPPE, C., 2001. *Bubble size measurement using wire-mesh sensors*. Flow Meas. Instrum. 12(4), 299-312.

REN, S., HE, K., GIRSHICK, R., SUN, J., 2017. *Faster R-CNN: Towards Real-Time Object Detection with Region Proposal Networks*. IEEE Trans. Pattern Anal. Mach. Intell. 39(06), 1137-1149.

SAAVEDRA MORENO, Y., BOURNIVAL, G., ATA, S., 2022. *Classification of flotation frothers – A statistical approach*. Chem. Eng. Sci. 248, 117252.

SCHMIDHUBER, J., 2015. *Deep learning in neural networks: An overview*. Neural Netw. 61, 85-117.

SOLVAY, 2018. *AeroFroth® 70 Safety Datasheet*.

TAO, D., 2005. *Role of Bubble Size in Flotation of Coarse and Fine Particles − A Review*. Sep. Sci. Technol. 39(4), 741-760.

VAZQUEZ, A., SANCHEZ, R. M., SALINAS-RODRÍGUEZ, E., SORIA, A., MANASSEH, R., 2005. *A look at three measurement techniques for bubble size determination*. Exp. Therm. Fluid Sci. 30(1), 49-57.

VINNETT, L., 2023. *A discussion on the limitations of image analysis for determining bubble size in industrial flotation when using algorithms successfully tested from idealized images*. Physicochem. Probl. Miner. Process. 59(5), 174474.

VINNETT, L., ALVAREZ-SILVA, M., 2015. *Indirect estimation of bubble size using visual techniques and superficial gas rate*. Miner. Eng. 81, 5-9.

VINNETT, L., CORNEJO, I., YIANATOS, J., ACUÑA, C., URRIOLA, B., GUAJARDO, C., ESTEBAN, A., 2022. *The correlation between macroscopic image and object properties with bubble size in flotation*. Minerals 12(12), 1528.

VINNETT, L., SOVECHLES, J., GOMEZ, C. O., WATERS, K. E., 2018. *An image analysis approach to determine average bubble sizes using one-dimensional Fourier analysis*. Miner. Eng. 126, 160-166.

VINNETT, L., URRIOLA, B., ORELLANA, F., GUAJARDO, C., ESTEBAN, A., 2022. *Reducing the presence of clusters in bubble size measurements for gas dispersion characterizations*. Minerals 12(9), 1148.

VINNETT, L., YIANATOS, J., ACUÑA, C., CORNEJO, I., 2022. *A method to detect abnormal gas dispersion conditions in flotation machines*. Minerals 12(2), 125.

VINNETT, L., YIANATOS, J., ARISMENDI, L., WATERS, K. E., 2020. *Assessment of two automated image processing methods to estimate bubble size in industrial flotation machines*. Miner. Eng. 159, 106636.

VINNETT, L. E., CONTRERAS, F. A., YIANATOS, J. B., 2009. *Bubble size analysis and boundary conditions for automatic control of industrial flotation cells*. IFAC Proc. 42(23), 161-166.

WANG, G., NGUYEN, A. V., MITRA, S., JOSHI, J. B., JAMESON, G. J., EVANS, G. M., 2016. *A review of the mechanisms and models of bubble-particle detachment in froth flotation*. Sep. Purif. Technol. 170, 155-172.

WANG, H., YANG, Y., DOU, G., LOU, J., ZHU, X., SONG, L., DONG, F., 2023. *A 3D reconstruction method of bubble flow field based on multi-view images by bi-direction filtering maximum likelihood expectation maximization algorithm*. Int. J. Multiph. Flow, 165, 104480.